# Investigation of Nonlinear Difference-Frequency Wave Excitation on a Semisubmersible Offshore-Wind Platform With Bichromatic-Wave CFD Simulations

## Preprint


Lu Wang,[1] Amy Robertson,[1] Jason Jonkman,[1] Yi-Hsiang Yu,[1] Arjen Koop,[2] Adrià Borràs Nadal,[3] Haoran Li,[4] Wei Shi,[5] Romain Pinguet,[6] Yang Zhou,[7] Qing Xiao,[7] Rupesh Kumar,[8] Hamid Sarlak[9]

*1 National Renewable Energy Laboratory*
*2 Maritime Research Institute Netherlands (MARIN)*
*3 IFP Energies Nouvelles (IFPEN)*
*4 Norwegian University of Science and Technology (NTNU)*
*5 Dalian University of Technology (DUT)*
*6 Principle Power, Inc. (PPI)*
*7 University of Strathclyde (UOS)*
*8 University of Ulsan (UOU)*
*9 Technical University of Denmark (DTU)*


*Presented at 3rd International Offshore Wind Technical Conference (IOWTC2021)*
*February 16–17, 2021*


**NREL is a national laboratory of the U.S. Department of Energy**
**Office of Energy Efficiency & Renewable Energy**
**Operated by the Alliance for Sustainable Energy, LLC**

This report is available at no cost from the National Renewable Energy Laboratory (NREL) at www.nrel.gov/publications.

Contract No. DE-AC36-08GO28308

**Conference Paper**
NREL/CP-5000-77014
April 2021

# Investigation of Nonlinear Difference-Frequency Wave Excitation on a Semisubmersible Offshore-Wind Platform With Bichromatic-Wave CFD Simulations

## Preprint

Lu Wang,[1] Amy Robertson,[1] Jason Jonkman,[1] Yi-Hsiang Yu,[1] Arjen Koop,[2] Adrià Borràs Nadal,[3] Haoran Li,[4] Wei Shi,[5] Romain Pinguet,[6] Yang Zhou,[7] Qing Xiao,[7] Rupesh Kumar,[8] Hamid Sarlak[9]

*1 National Renewable Energy Laboratory*
*2 Maritime Research Institute Netherlands (MARIN)*
*3 IFP Energies Nouvelles (IFPEN)*
*4 Norwegian University of Science and Technology (NTNU)*
*5 Dalian University of Technology (DUT)*
*6 Principle Power, Inc. (PPI)*
*7 University of Strathclyde (UOS)*
*8 University of Ulsan (UOU)*
*9 Technical University of Denmark (DTU)*

**Suggested Citation**
Wang, Lu, Amy Robertson, Jason Jonkman, Yi-Hsiang Yu, Arjen Koop, Adrià Borràs Nadal, Haoran Li, Wei Shi, Romain Pinguet, Yang Zhou, Qing Xiao, Rupesh Kumar, Hamid Sarlak. 2021. *Investigation of Nonlinear Difference-Frequency Wave Excitation on a Semisubmersible Offshore Wind Platform With Bichromatic-Wave CFD Simulations: Preprint*. Golden, CO: National Renewable Energy Laboratory. NREL/CP-5000-77014. https://www.nrel.gov/docs/fy21osti/77014.pdf.

**NREL is a national laboratory of the U.S. Department of Energy**
**Office of Energy Efficiency & Renewable Energy**
**Operated by the Alliance for Sustainable Energy, LLC**

This report is available at no cost from the National Renewable Energy Laboratory (NREL) at www.nrel.gov/publications.

Contract No. DE-AC36-08GO28308

**Conference Paper**
NREL/CP-5000-77014
April 2021

National Renewable Energy Laboratory
15013 Denver West Parkway
Golden, CO 80401
303-275-3000 • www.nrel.gov

# INVESTIGATION OF NONLINEAR DIFFERENCE-FREQUENCY WAVE EXCITATION ON A SEMISUBMERSIBLE OFFSHORE-WIND PLATFORM WITH BICHROMATIC-WAVE CFD SIMULATIONS

**Lu Wang[1], Amy Robertson[1], Jason Jonkman[1], Yi-Hsiang Yu[1], Arjen Koop[2], Adrià Borràs Nadal[3], Haoran Li[4], Wei Shi[5], Romain Pinguet[6], Yang Zhou[7], Qing Xiao[7], Rupesh Kumar[8], Hamid Sarlak[9]**

[1]National Renewable Energy Laboratory (NREL), Golden, CO
[2]Maritime Research Institute Netherlands (MARIN), Wageningen, Netherlands
[3]IFP Energies nouvelles (IFPEN), Rueil-Malmaison, France
[4]Norwegian University of Science and Technology (NTNU), Trondheim, Norway
[5]Dalian University of Technology (DUT), Dalian, China
[6]Principle Power, Inc. (PPI), Emeryville, CA
[7]University of Strathclyde (UOS), Glasgow, UK
[8]University of Ulsan (UOU), Ulsan, South Korea
[9]Technical University of Denmark (DTU), Kongens Lyngby, Denmark

## ABSTRACT

*The natural surge and pitch frequencies of semisubmersible offshore wind platforms are typically designed to be below the wave frequencies to avoid direct excitation. However, surge or pitch resonance can be excited by the nonlinear low-frequency loads generated by irregular incident waves. Second-order potential-flow models with added Morison drag have been found to underpredict this low-frequency excitation and response. As part of the OC6 project[1], the authors performed computational fluid dynamics (CFD) simulations to enable a better understanding of the low-frequency loads and the limitations of lower-fidelity models. The focus of this paper is to set up a computationally cost-effective CFD simulation of a fixed semisubmersible platform to investigate nonlinear difference-frequency loads and establish the corresponding uncertainty in the results. Because of the high computing cost, CFD simulations of irregular waves can be challenging. Instead, simulations were performed with bichromatic waves having a shorter repeat period. A preliminary comparison with quadratic transfer functions from second-order potential-flow theory shows that CFD models consistently predict higher nonlinear wave loads at the difference frequency, likely because of flow separation and viscous drag not accounted for in potential-flow theory.*

Keywords: semisubmersible, bichromatic waves, difference frequency, QTF, low frequency, 2nd order, wave load, computational fluid dynamics, CFD, IEA wind, OC6.

## 1. INTRODUCTION

As the support structure of a floating offshore wind turbine, a semisubmersible platform has several advantages, which include the use of conventional mooring and possible quayside assembly and maintenance. Semisubmersibles are typically designed to have very low surge and pitch natural frequencies to avoid direct wave excitation. However, small nonlinear wave forces and moments at low frequencies can still induce large surge and pitch motion at the natural frequencies [1, 2]. The low-frequency load and response of the platform are frequently underpredicted by current engineering modeling tools for floating offshore wind systems, presenting a major obstacle to the accurate estimation of the ultimate and fatigue loads of floating wind turbines.

The issue with underpredicting low-frequency wave excitation and platform response was identified in the previous Offshore Code Comparison Collaboration, Continued, with Correlation (OC5) project under Task 30 of the International Energy Agency (IEA) Wind [3]. Therefore, Phase I of the new OC6 (OC5 with unCertainty) project is dedicated to better understanding this issue and improving the predictions of the hydrodynamic load on, and the response of, a semisubmersible

[1] Project under IEA Wind Task 30: Offshore Code Comparison Collaboration, Continued, with Correlation and unCertainty (OC6).

platform at low frequencies. In the first part of OC6 Phase I, extensive investigations using simplified engineering models identified the inclusion of full quadratic transfer functions (QTFs) from the second-order potential-flow theory as one of the model features that consistently improves the low-frequency predictions. In comparison, Newman's approximation was found to underestimate the second-order response in some cases [4, 5]. Nevertheless, the global load and response near the surge and pitch resonance frequencies were still significantly underpredicted in irregular sea states with a full QTF [5, 6]. Second-order potential-flow models augmented by Morison drag with a strip-theory formulation have also been evaluated. While a large drag coefficient was found to increase the low-frequency wave excitation on a fixed platform, the motion response under floating configuration became severely underpredicted [5, 6].

To understand the reasons for the underprediction of the low-frequency load and response in engineering-level tools, the OC6 project is setting up higher-fidelity simulations in computational fluid dynamics (CFD) tools to investigate the phenomenon. Floating offshore wind turbines have already been extensively studied using CFD to varying degrees of complexity. For example, Tran et al. investigated the free-decay motion of the DeepCwind platform and its response to regular incident waves using CFD [7]. One interesting observation from the study is that nearly identical results for surge free-decay motion can be obtained both with and without the shear stress transport $k$-$\omega$ turbulence model. On the other hand, the $k$-$\epsilon$ model was found to result in excessive viscous damping. Other researchers also obtained mostly consistent predictions of wave forces on the platform from simulations both with and without turbulence models under certain wave conditions (see e.g., [8, 9]). Ren et al. investigated the motion of a tension-leg platform in extreme regular waves [10]. Burmester et al. simulated the surge decay of a moored semisubmersible offshore wind turbine using CFD with a special focus on the estimation of surge damping [11]. Bozonnet and Emery, on the other hand, focused on the forced heave and pitch oscillation of a floating wind platform with heave plates to extract the relevant hydrodynamic coefficients for potential flow-based engineering models [12]. Subsequent CFD simulations were expanded to also include the rotating wind turbine to investigate the platform response under combined wind-wave effects with a focus on free-decay motion and response to regular-wave excitation [13, 14, 15].

Different from the aforementioned CFD investigations focusing on the free-decay motion and the response to regular waves, the current work is primarily concerned with the nonlinear difference-frequency loads experienced by the offshore wind platform. As an initial investigation, only a captive platform fixed in place is considered in this paper. One major challenge associated with CFD is the long computing time needed to simulate the full 3-hour time window typically required by irregular sea states. Therefore, the current CFD investigation instead focuses on bichromatic waves with short repeat periods, which significantly reduces the computing time, allowing more wave cases to be simulated for a more comprehensive understanding of the nonlinear low-frequency effects [16]. Furthermore, the difference-frequency loads obtained from the bichromatic-wave CFD simulations can be directly compared to potential-flow QTFs to identify the limitations of second-order potential-flow theory. Several previous studies also leveraged the convenience offered by bichromatic waves when investigating nonlinear wave loads and responses of offshore platforms and ships (see e.g., [4, 17]). In this paper, a baseline setup of the bichromatic-wave CFD simulation, including meshing and numerical settings, is documented along with convergence studies and uncertainty estimates. The baseline setup was provided to each OC6 participant for reference. Using their own meshing tools and CFD software, each participant independently carried out the simulation for the same bichromatic-wave case with varying degrees of modification to the baseline setup depending on the capabilities of the software used, the available computing resources, and past experience. The CFD results provided by the various OC6 participants were then gathered and compared with each other and to potential-flow predictions.

## 2. PROBLEM DESCRIPTION

In the current study, we used a geometrically simplified version of the OC5-DeepCwind semisubmersible platform [3]. The platform consists of three identical columns, one upstream and two downstream, placed at the corners of an equilateral triangle. The center-to-center distance between each column is $L = 50$ m. Each column has a radius of 6 m and a draft of 14 m. Below each column, a heave plate/base column with a radius of 12 m and height 6 m is attached. Crossmembers (pontoons and braces) connecting the columns were all omitted, along with the central column.

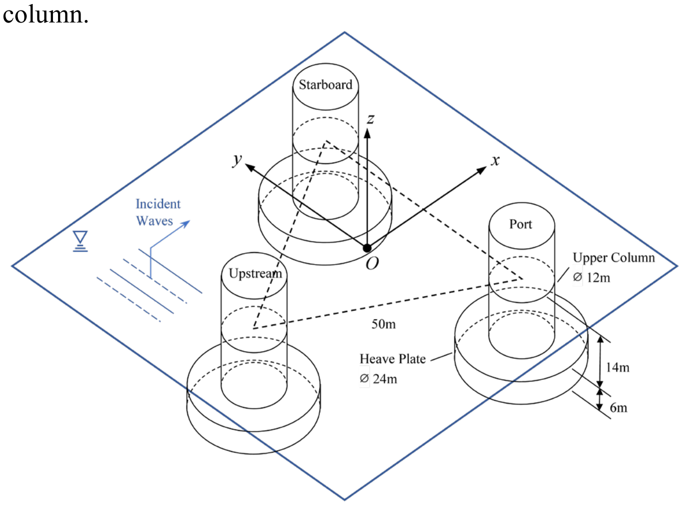


Figure 1. Geometry of the semisubmersible platform and the adopted coordinate system.

The origin of the coordinate system is located on the free surface at the geometric center of the equilateral triangle. The $+x$-axis is in the direction of wave propogation, and the $+z$-axis points upward. Following the right-hand convention, the $+y$-axis points toward the starboard. The platform geometry and the adopted coordinate system are both shown in Figure 1.

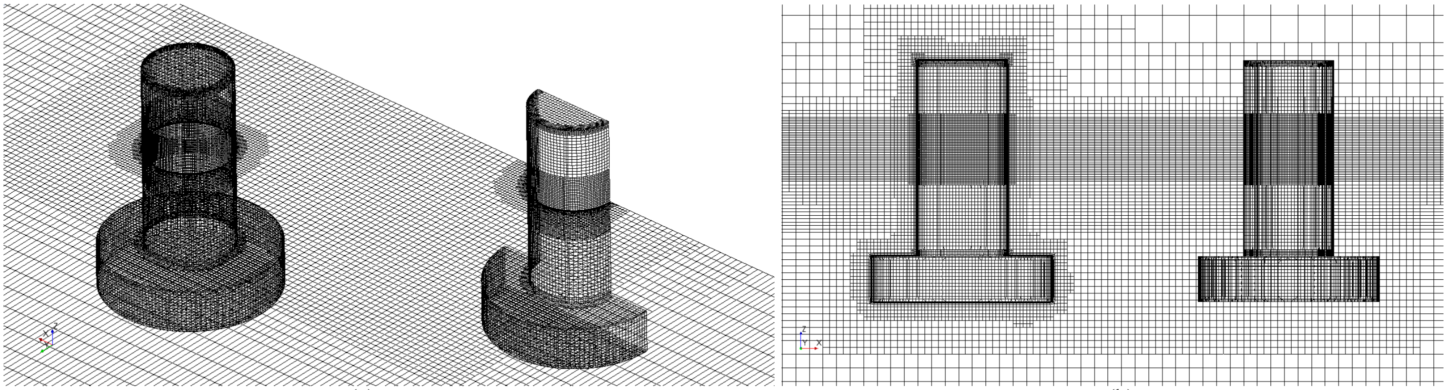

Figure 2. Baseline mesh for the bichromatic-wave simulation. (a) Column surface mesh and waterplane mesh. (b) Column surface mesh and platform center-plane mesh.

The semisubmersible platform is fixed in place and subjected to the load from bichromatic incident waves. The linear-wave (first-order) parameters for the two components of the incident waves are listed in Table 1. The mean water depth is 290 m, and the deep-water limit applies to both primary wave components. The two wave components yield a difference frequency of $f_d = 0.032$ Hz, which is approximately the pitch natural frequency of the OC5-DeepCwind semisubmersible [3]. With linear-wave approximation, the bichromatic waves repeat every $T_R = 249.9$ s.

All dimensional values presented in this paper are given at full scale; however, because we would eventually like to validate our CFD results against wave-tank measurements made with the same simplified model geometry shown in Figure 1, the simulations were all carried out at a 1:50 model scale instead, with the results scaled up based on Froude scaling during postprocessing.

Table 1. Two components of the bichromatic incident waves.

| Wave | Period | Frequency | Wavelength | Amplitude |
|---|---|---|---|---|
| 1 | $T_1$=11.900 s | $f_1$=0.084 Hz | $\lambda_1$=221 m | $A_1$=1.755 m |
| 2 | $T_2$=8.6172 s | $f_2$=0.116 Hz | $\lambda_2$=116 m | $A_2$=1.745 m |

## 3. NUMERICAL METHOD AND SETUP

All participants of the OC6 project solved the incompressible Navier-Stokes equation and the continuity equation using the finite-volume method and adopted the volume-of-fluid (VOF) formulation to model the free-surface flow. Furthermore, the standard turbulence models were found to cause excessive dissipation of the surface waves over time, resulting in a steady and continuous drop in wave-exciting forces. Therefore, all OC6 participants performed the simulation without any turbulence model.

The boundary conditions used are largely consistent across all participants. Flow velocity and the free-surface level at the upstream boundary were prescribed based on the linear superposition of the two wave components. An upstream wave-forcing zone was also used by some participants to prevent wave reflection from the upstream boundary. A symmetry, free-slip, or no-slip condition was used on the two vertical side boundaries. If the simulation was performed on a half domain to exploit the port-starboard symmetry, the platform center plane was treated as a symmetry plane. The bottom was treated as either a no-slip or a free-slip surface. A wave-damping/relaxation zone typically at least $2\lambda_1$ long was placed next to the downstream boundary to minimize wave reflection. The downstream boundary was treated as a pressure inlet/outlet with hydrostatic pressure specified or a zero-gradient boundary if a downstream wave-damping zone was used. Alternatively, the incident wave-field velocity and free-surface level can be prescribed on the downstream boundary to be consistent with a downstream wave-relaxation zone. Maritime Research Institute Netherlands (MARIN) also utilized a nonreflecting boundary condition for the difference-frequency waves (see Section 3.2). The top boundary was treated as a constant pressure inlet/outlet. A no-slip condition was enforced on the solid surface of the platform by all participants except IFP Energies nouvelles (see Section 3.2).

### 3.1 Baseline Numerical Setup

To ensure a level of consistency in the quality of the numerical results across all participants, we specified baseline domain size, grid resolution, time step, and numerical discretization schemes. The exact setup of each participant deviated from the baseline to varying degrees depending on the available computing resources and the capabilities of the software used.

The baseline numerical domain is 2004 m long (approximately $9\lambda_1$), 100 m wide from the platform center plane (2.7 times the maximum platform half width measured to the edge of the heave plate), and 390 m tall. The upstream boundary is 442 m ($2\lambda_1$) from the platform center ($x = 0$).

Because only a fixed platform was considered in the current work, dynamic mesh or overset grids were not required, and only a single fixed mesh was built. Nevertheless, for the sake of brevity, we describe the mesh as having two separate regions: a background wave mesh that encompasses the entire domain, and a platform mesh that covers the underwater region near the platform. A trimmed mesh with predominantly hexahedral cells was used outside the boundary-layer region. The cell sizes are given as multiples of the reference sizes $h_w$ for the wave mesh and $h_p$ for the submerged portion of the platform mesh. For the baseline case, we have $h_w = 0.45$ m $\approx 2(A_1 + A_2)/15.6$ and $h_p = 0.9$ m $\approx D/26.7$, where $D = 24$ m is the diameter of the heave plate.

To adequately resolve the bichromatic incident waves, the background wave mesh was refined near and right below the free surface. The regions of refinement, given by ranges of $z$-coordinates, and the corresponding cell sizes in the $x$-, $y$-, and $z$-directions, $\Delta x$, $\Delta y$, and $\Delta z$, are listed in Table 2. Away from the refinement regions, the mesh gradually transitioned to large isotropic cells ($16h_w$ wide). There was no variation in cell size in the $x$- and $y$-directions except in the downstream damping zone where the mesh was suitably coarsened.

Table 2. Refinement of background wave mesh.

| $z$ [m] | $\Delta x$ | $\Delta y$ | $\Delta z$ |
|---|---|---|---|
| [-4, 4.5] | $2h_w$ | $8h_w$ | $0.5h_w$ |
| [-10, -4] | $4h_w$ | $8h_w$ | $1h_w$ |
| [-25, -10] | $4h_w$ | $8h_w$ | $2h_w$ |

Near the platform, the mesh was further refined to better resolve wave diffraction and flow separation from the platform. The regions of refinement and cell sizes for the platform mesh are listed in Table 3. To avoid spurious wave reflection, the cell sizes near the free surface in the $x$- and $z$-directions were kept consistent with the background wave mesh while $\Delta y$ was reduced to be the same as $\Delta x$ to better resolve the diffracted waves. Below the free surface, a uniform isotropic mesh was used to better capture any flow separation from the columns and the sharp corners of the heave plates.

The surface of the platform was discretized into square patches with side $0.5h_p$, and a 10-layer boundary-layer mesh that was 0.4 m thick was extruded from the surface. The thickness of each layer was increased by a constant expansion ratio from the previous with the thinnest layer next to the solid surface being 1 mm thick. The baseline mesh for a half domain, shown in Figure 2, comprised 4.2 million cells in total.

Table 3. Refinement of platform mesh.

| $x$ [m] | $y$ [m] | $z$ [m] | $\Delta x$ | $\Delta y$ | $\Delta z$ |
|---|---|---|---|---|---|
| [-47.5, 35] | [0, 45] | [-4, 4.5] | $2h_w$ | $2h_w$ | $0.5h_w$ |
| [-45, 30] | [0, 40] | [-25, -4] | $h_p$ | $h_p$ | $h_p$ |

We used second-order implicit time integration with a baseline time step of $\Delta t = T_2/1030$. This choice of time step resulted in wave-based Courant numbers of 0.13 and 0.17 for the first and second wave components, respectively. All spatial discretization schemes were also formally second order. The numerical simulation was carried out for $2.5T_R$, equal to $52.5T_1$ or $72.5T_2$.

It should be noted that the adopted baseline grid and time step likely do not yield fully converged results. However, the goal of the current work is not to simply present a fully converged solution for the single bichromatic-wave case considered. Rather, we would like to determine whether it is possible to perform such simulations for a host of similar cases under a reasonable amount of time with an acceptable level of uncertainty that renders the results useful for engineering design purposes. In Section 4, results from several repeated simulations with modified numerical configurations are presented to estimate the uncertainty associated with the baseline setup.

### 3.2 Numerical Setups of OC6 Participants

OC6 participants that provided simulation results for the load case defined here included the Technical University of Denmark (DTU), Dalian University of Technology (DUT), IFP Energies nouvelles (IFPEN), the Maritime Research Institute Netherlands (MARIN), the National Renewable Energy Laboratory (NREL), the Norwegian University of Science and Technology (NTNU), Principle Power Inc. (PPI), the University of Strathclyde (UOS), and the University of Ulsan (UOU).

IFPEN performed the simulation using OpenFOAM [18] with the waves2Foam toolbox [19] on two different full-domain meshes. The first computational mesh lacked an extruded region for the boundary layer. The boundary condition on the platform surface was also changed to free slip. This is the same approach adopted in [20]. Because we expect viscous effects to manifest primarily through flow separation from the sharp corners of the heave plates, we anticipate the effect of not resolving the boundary layer on the global forces and moments to be limited. The second mesh is similar to the first one except a five-layer boundary-layer mesh was extruded from the floater surface. With the second mesh, the boundary condition on the floater surface was changed to no-slip.

MARIN generated a half-domain mesh using HEXPRESS [21] following the grid-size and domain-size guidelines provided in Section 3.1. The simulation was performed using ReFRESCO [22] with the ReFRICS interface-capturing scheme [23]. Furthermore, a nonreflective Sommerfeld-type boundary condition was applied on the inlet and outlet to minimize the reflection of the long difference-frequency free waves (see Section 4.1).

NREL results were obtained with the commercial CFD software STAR-CCM+ [24]. Because of port-starboard symmetry, the simulation was carried out with only the starboard half of the platform. The baseline setup described in Section 3.1 was adopted without modification.

NTNU performed the simulation with OpenFOAM [18] and waves2Foam [19]. The baseline setup was adopted except that the cell size in the $y$-direction, $\Delta y$, on the free surface (first mesh refinement region in Table 2) was halved.

Both DUT and UOU performed the simulation on the same half-domain mesh used by NREL with STAR-CCM+ [24] and ANSYS Fluent [25], respectively. Furthermore, UOU used a slightly larger time step of $\Delta t = T_2/862$.

DTU, PPI, and UOS all performed the simulation on the first full-domain mesh built by IFPEN using OpenFOAM [18] with the waves2Foam toolbox [19]. DTU adopted the first-order implicit Euler method for time integration rather than a second-order implicit method prescribed by the baseline configuration. UOS, on the other hand, adopted a much finer time step of $\Delta t = T_2/2438$.

Additional details on the CFD setups adopted by the various participants are summarized in Table A.1 in the Appendix.

## 4. ANALYSIS AND PROCESSING OF NUMERICAL RESULTS

To ascertain the quality of the generated waves, the bichromatic incident waves were simulated first in 2D without the platform present. Subsequently, we performed simulations with the fixed platform to obtain the wave loads on the platform. Furthermore, NREL has conducted a convergence study by repeating the simulation several times with different time steps, grid sizes, and domain widths to estimate the uncertainty in the obtained wave loads, both at the wave frequencies and at the difference frequency. Because of the number of simulations needed, and the computing resources required, the systematic numerical uncertainty analysis was performed for the NREL results only. In this section, this uncertainty estimation is presented. The results from all OC6 participants are compared to each other in Section 5 as well as to second-order potential-flow predictions.

### 4.1 Bichromatic Incident Waves

The bichromatic incident waves were first simulated without the presence of the platform. A 2D mesh with a resolution in the $xz$-plane equivalent to the baseline mesh described in Section 3 was used for the wave-only simulations. The wave-elevation time series at various $x$-positions along the domain were recorded, and Fast Fourier Transforms (FFTs) were performed on the time series from the last available repeat period, $t \in [1.5T_R, 2.5T_R)$, to obtain the amplitudes at the wave frequencies and the difference frequency. The wave amplitudes specified in the upstream boundary condition were adjusted iteratively until the target wave amplitudes given in Table 1 were obtained to within a 3% difference at $x = 0$ with the baseline grid and time step. The remaining minor differences were accounted for by normalizing the results based on the actual obtained wave amplitudes at $x = 0$ instead of the target amplitudes. All OC6 project participants independently went through the same wave-calibration process to ensure consistent incident waves.

To investigate grid convergence, a fine and a coarse mesh were constructed by halving and doubling the reference cell size $h_w$ while maintaining the ratios shown in Table 2. Temporal convergence was investigated by simulating the waves on the baseline mesh using either half or double the baseline time step. The inlet wave amplitudes calibrated for the baseline grid and time step were consistently used in all runs of the convergence study.

The wave amplitudes at the two wave frequencies measured at $x = 0$ (the platform center location) are listed in Table 4. For reference, the maximum local convective Courant number encountered is also listed for each configuration. When computing the maximum Courant number, the initial transient phase, which had a higher Courant number, was excluded. Furthermore, we found a few cells on the downstream boundary having a significantly higher Courant number (approximately doubles the maximum elsewhere), likely because of the truncated cell size. Because these cells were located deep inside the damping zone, they were also excluded.

Overall, the wave amplitudes show weak dependence on time step and cell size for the range of time step and cell size considered. The convergence with cell size was not monotonic. In fact, the simulation with the largest cell size, $h_w = 0.9$ m, was likely outside the asymptotic convergence regime. Nevertheless, the level of convergence for the wave-only case was considered adequate with the baseline cell size of $h_w = 0.45$ m and time step of $\Delta t = T_2/1030$; further reducing the time step or cell size did not significantly change the wave amplitudes.

The wave amplitudes obtained with the baseline grid and time step at various $x$-positions are presented in Figure 3. Outside the damping zone, the amplitude of the low-frequency ($f_1$=0.084 Hz) waves remained relatively constant over the entire domain. Meanwhile, some dissipation can be observed for the high-frequency ($f_2$=0.116 Hz) waves. The slight decrease in wave amplitude downstream was compensated by adjusting the inlet wave amplitudes, as discussed previously.

Table 4. Wave amplitudes at $x = 0$.

| Wave | $h_w = 0.45$ m $\Delta t = T_2/515$ | $h_w = 0.45$ m $\Delta t = T_2/1030$ | $h_w = 0.45$ m $\Delta t = T_2/2060$ |
|---|---|---|---|
| 1 | $A_1 = 1.737$ m | $A_1 = 1.756$ m | $A_1 = 1.765$ m |
| 2 | $A_2 = 1.773$ m | $A_2 = 1.794$ m | $A_2 = 1.822$ m |
| Max. Courant # | 0.28 | 0.15 | 0.09 |
| Wave | $h_w = 0.9$ m $\Delta t = T_2/1030$ | $h_w = 0.45$ m $\Delta t = T_2/1030$ | $h_w = 0.225$ m $\Delta t = T_2/1030$ |
| 1 | $A_1 = 1.761$ m | $A_1 = 1.756$ m | $A_1 = 1.762$ m |
| 2 | $A_2 = 1.822$ m | $A_2 = 1.794$ m | $A_2 = 1.814$ m |
| Max. Courant # | 0.09 | 0.15 | 0.28 |

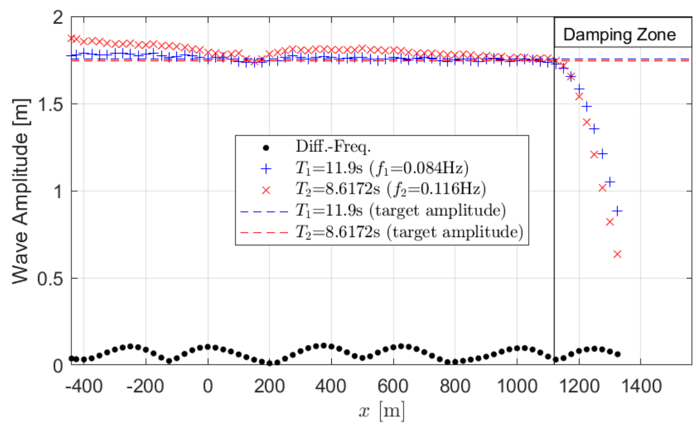


Figure 3. Wave amplitudes at various $x$-positions obtained with the baseline grid and time step.

The wave amplitude at the difference frequency ($f_d$) varied strongly with $x$. Upon closer inspection, the amplitude modulation was found to be the result of the superposition of three different wave components at the difference frequency: incident bound waves, incident free waves, and reflected free waves from the downstream boundary. The incident bound waves came from the nonlinear interactions between the two primary wave components. The bound waves do not satisfy the linear dispersion relation and have a wavenumber $k_b = |k_1 - k_2|$, where $k_1$ and $k_2$ are the wavenumbers of the two primary waves. The incident free waves, on the other hand, were likely generated by imperfect wave-making at the upstream boundary. While likely nonlinear in origin, the free waves satisfy the linear-wave dispersion relation. The low frequency of the free waves leads to a very long wavelength of $\lambda_d$ =1336 m, which is comparable to the domain length and significantly longer than the downstream damping zone. As a result, the incident free waves cannot be effectively absorbed, resulting in reflected free waves. Strictly speaking, there should also be reflected bound waves. However, because the two primary wave components were effectively absorbed by the damping zone, the reflected bound waves were negligible.

By adapting the wave-splitting method from [26], we can reliably decompose the three wave components at the difference frequency. The complex difference-frequency wave amplitudes, $A_{d1}, A_{d2}, \dots, A_{dn}$, at $n$ different $x$-positions, $x_1, x_2, \dots, x_n$, can be assumed to have the form:

$$A_{dj} = \zeta_{if} \mathrm{e}^{-\mathrm{i}k_d x_j} + \zeta_{rf} \mathrm{e}^{\mathrm{i}k_d x_j} + \zeta_{ib} \mathrm{e}^{-\mathrm{i}k_b x_j},\ j = 1,2,\dots,n \quad (1)$$

where $\mathrm{i} = \sqrt{-1}$ and $\zeta_{if}$, $\zeta_{rf}$, and $\zeta_{ib}$ are the constant and complex amplitudes of the incident free waves, reflected free waves, and the incident bound waves, respectively. The wavenumber of the difference-frequency free waves, $k_d$, can be determined from the linear-wave dispersion relation. If $A_{dj}$ is known at $n \geq 3$ different $x$-positions, as in Figure 3, a linear system of equations can be formed to solve for $\zeta_{if}$, $\zeta_{rf}$, and $\zeta_{ib}$:

$$\begin{bmatrix} \mathrm{e}^{-\mathrm{i}k_d x_1} & \mathrm{e}^{\mathrm{i}k_d x_1} & \mathrm{e}^{-\mathrm{i}k_b x_1} \\ \vdots & \vdots & \vdots \\ \mathrm{e}^{-\mathrm{i}k_d x_n} & \mathrm{e}^{\mathrm{i}k_d x_n} & \mathrm{e}^{-\mathrm{i}k_b x_n} \end{bmatrix} \begin{bmatrix} \zeta_{if} \\ \zeta_{rf} \\ \zeta_{ib} \end{bmatrix} = \begin{bmatrix} A_{d1} \\ \vdots \\ A_{dn} \end{bmatrix}, \quad (2)$$

assuming the choices of $x_j$ do not result in a singular system. A minimum of $n = 3$ is needed to solve Eq. (2); however, it is more reliable to have $n \gg 3$ and solve Eq. (2) in the least-square sense. In this paper, the wave amplitudes at 28 different $x$-positions equally spaced between $x = -275$ m to $400$ m were used to decompose the difference-frequency waves. The results were not sensitive to the choices of $x$-positions so long as they were not too close to the upstream boundary or the downstream damping zone. For the waves shown in Figure 3, we have $|\zeta_{if}| = 0.0543$ m, $|\zeta_{rf}| = 0.0167$ m, and $|\zeta_{ib}| = 0.0442$ m. The value of $|\zeta_{ib}|$ is in reasonable agreement with the theoretical value given by the second-order potential-flow theory, $A_1 A_2 |k_1 - k_2|/2 = 0.0408$ m [27]. This agreement was consistently observed for several different bichromatic-wave cases we have investigated.

The amplitude of the free waves at the difference frequency were found to be sensitive to the overall domain length. With the baseline numerical setup (i.e., upstream velocity inlet with downstream wave-damping zone), we observed resonance behavior of the difference-frequency free waves when the overall domain length was an odd multiple of $\lambda_d/4$. Because we are interested in obtaining results for pure bichromatic waves, resonance should be avoided to minimize the impact of the free waves on the difference-frequency wave loads. Therefore, we used an overall domain length of 2004 m= $6/4\lambda_d$.

### 4.2 Wave Excitation on a Fixed Platform

With the quality of the bichromatic incident waves evaluated, we performed 3D simulations with the semisubmersible platform in waves. The wave-induced surge force, $F_x$, heave force, $F_z$, and pitch moment about the $y$-axis, $M_y$, on the fixed semisubmersible platform were evaluated from the CFD results. The quantities of interest are the difference-frequency amplitudes of $F_x$ and $M_y$, and, to a much lesser degree, that of $F_z$ because the heave natural frequency of semisubmersibles is typically in the wave-frequency region as opposed to the low-frequency region. The wave-frequency amplitudes of the wave excitation are also presented for completeness. The load amplitudes were obtained by performing an FFT on a section of the force/moment time series from a time window $T_R$ wide. The FFT of the surge force computed from the time window $t \in [1.5T_R, 2.5T_R)$ is shown in Figure 4.

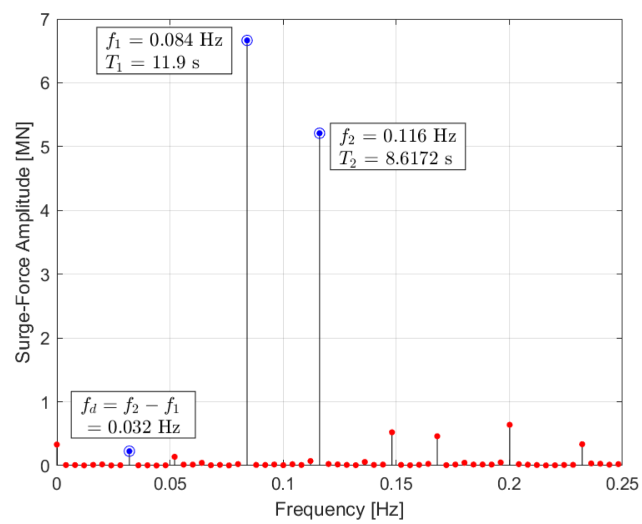


Figure 4. Amplitude of surge force obtained by performing FFT over $t \in [1.5T_R, 2.5T_R)$ with frequency components of interest labeled.

In the rest of this paper, all amplitudes of wave-exciting forces and moments are normalized by the factors listed in Table 5, where $\rho$, $g$, $L$, and $A_{wp}$ are the water density, gravitational acceleration, center-to-center distance between columns, and the waterplane area of the platform, respectively.

The obtained force/moment amplitudes fluctuate slightly depending on the time window used for the FFT analysis. To investigate the level of variation, the force amplitude was calculated from the FFT of the force time series over a sliding time window, $t \in [t_s, t_s + T_R)$, where $t_s$ is the start of the window. Figure 5 shows how the difference-frequency amplitude of $F_x$ changes with the sliding window. Initial transient behavior is observed up to $t_s/T_R = 0.5$, after which the normalized force amplitude fluctuates about a mean value of 0.84. To avoid the initial transient phase, we consistently used the last available time window, $t \in [1.5T_R, 2.5T_R)$, to compute the force/moment amplitudes in all subsequent analysis.

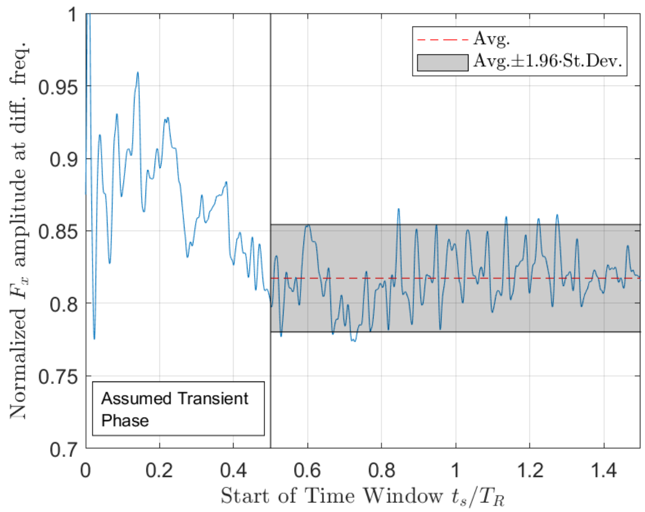

Figure 5. Variation of surge-force amplitude at the difference frequency with time window.

Table 5. Normalization factors for force/moment amplitudes.

| | Difference Frequency ($f_d$) | 1st Wave Freq. ($f_1$) | 2nd Wave Freq. ($f_2$) |
|---|---|---|---|
| $F_x$ | $\rho g A_{wp} A_1 A_2 (k_1 - k_2)$ | $2\rho g A_{wp} A_1$ | $2\rho g A_{wp} A_2$ |
| $F_z$ | $0.5\rho g A_{wp} A_1 A_2 (k_1 - k_2)$ | $\rho g A_{wp} A_1$ | $\rho g A_{wp} A_2$ |
| $M_y$ | $0.5\rho g L A_{wp} A_1 A_2 (k_1 - k_2)$ | $\rho g L A_{wp} A_1$ | $\rho g L A_{wp} A_2$ |

All force/moment amplitudes computed using the baseline numerical configuration and the final time window of $t \in [1.5T_R, 2.5T_R)$ are listed in Table 6.

Table 6. Normalized wave-load amplitudes computed using the baseline configuration.

| | Diff. Freq. ($f_d$) | 1st Wave Freq. ($f_1$) | 2nd Wave Freq. ($f_2$) |
|---|---|---|---|
| $F_x$ | 0.8146 | 0.5562 | 0.4256 |
| $F_z$ | 1.7112 | 0.4414 | 0.4104 |
| $M_y$ | 1.6291 | 0.3924 | 0.4294 |

### 4.2.1 Uncertainty in Wave Forces and Moments

One major objective of the current work is to estimate the uncertainties in the predicted wave-exciting forces and moments on the semisubmersible platform subjected to bichromatic incident waves, especially in the wave loads at the difference frequency. Although there are potentially many sources of errors and uncertainties, the following three were considered to be the major ones: numerical uncertainty dominated by temporal and spatial discretization errors ($U_1$), modeling uncertainty caused by the finite numerical domain size ($U_2$), and, finally, statistical uncertainty associated with the minor fluctuation of force/moment amplitudes over analysis time ($U_3$), as demonstrated in Figure 5. The three sources of uncertainty are distinct in nature and were assumed independent. Therefore, the total uncertainty can be estimated as $U_{tot} = (\sum_{i=1}^{3} U_i^2)^{1/2}$.

*Numerical uncertainty from discretization error*

Temporal and spatial convergence can be evaluated together by maintaining an appropriate ratio between the time step and cell size during mesh refinement and coarsening. However, for more flexibility, we opted to perform separate investigations on the effect of time step and grid size. To estimate the temporal discretization error, the simulation was repeated with the baseline mesh using four increasingly finer time steps. The finest temporal resolution was achieved using an adaptive time-step solver to limit the convective Courant number to below 0.5. The resulting mean time step was approximately $\overline{\Delta t} = T_2/5390$. With the exception of the surge-force amplitude at the higher second wave frequency ($f_2$), monotonic convergence in time was observed for all quantities listed in Table 6. As an example, the pitch-moment amplitudes at the difference and wave frequencies are shown in Figure 6 for the four different time steps considered. The normalized difference-frequency amplitudes are scaled by a factor of 0.1 to fit better with the wave-frequency amplitudes in the same plot. For reference, the predictions from linear potential-flow theory are also included for the two primary wave frequencies.

To fully exploit the observed monotonic convergence, we estimated the uncertainty associated with temporal discretization using the method based on Richardson extrapolation [28]. The standard power-law error estimator was adopted for the discretization error:

$$\phi_i - (\phi_0 + e_0) = \delta_{RE} = \alpha_t (\Delta t)_i^{p_t} \quad (3)$$

where $\phi_i$ is a scalar quantity of interest obtained using the $i$th choice of time step. The exact value of the same quantity obtained at the limit of infinite temporal and spatial resolution is given by $\phi_o$. The constant $e_0$ represents the spatial discretization error associated with the baseline grid. The three constants $(\phi_0 + e_0)$, $\alpha_t$, and $p_t$ were determined using the available results obtained with different time steps. More specifically, the constants were chosen to minimize the function:

$$S(\phi_0 + e_0, \alpha_t, p_t) = \sqrt{\sum_{i=1}^{n_t} \left[\phi_i - (\phi_0 + e_0 + \alpha_t (\Delta t)_i^{p_t})\right]^2} \quad (4)$$

where $n_t = 4$ is the number of different time steps used. Following the recommendation given in [28], the uncertainty resulting from temporal discretization was estimated as:

$$U_{\Delta t} = \begin{cases} \min(1.25|\delta_{RE}| + U_s, 1.25\Delta_M) & \text{for } 0 < p_t \le 0.95 \\ 1.25|\delta_{RE}| + U_s & \text{for } 0.95 < p_t < 2.05 \\ \max(1.25|\delta_{RE}^*| + U_s, 1.25\Delta_M) & \text{for } p_t \ge 2.05 \end{cases} \quad (5)$$

where $U_s$ is the standard deviation of the least-squares fit [29]:

$$U_s = \sqrt{\frac{\sum_{i=1}^{n_t} \left[\phi_i - (\phi_0 + e_0 + \alpha_t (\Delta t)_i^{p_t})\right]^2}{n_t - 3}}. \quad (6)$$

The error estimate, $\delta_{RE}^*$, is obtained by setting the order of convergence, $p_t$, to the theoretical value of 2. The data range, $\Delta_M$, is the maximum difference in $\phi_i$ across all available simulations:

$$\Delta_M = \max(|\phi_i - \phi_j|) \text{ for } 1 \le i, j \le n_t. \quad (7)$$

If the convergence is not monotonic, the range-based estimate for uncertainty is used [28, 30]:

$$U_{\Delta t} = 3\Delta_M \quad (8)$$

which is approximately consistent with a 95% confidence interval [30].

The Richardson extrapolation for the normalized pitch moment at the difference frequency is shown in Figure 7. The CFD results obtained with the four different time steps are shown as red crosses along with the uncertainty intervals estimated using Eq. (5). The time-step size is normalized by the smallest time step of $\Delta t_{min} = T_2/5390$. Monotonic convergence in time is observed. However, the order of convergence, $p_t$, obtained by minimizing the function in Eq. (4) was greater than 2.05. Therefore, the extrapolation was performed instead with $p_t = 2$ to obtain $\delta_{RE}^*$. The estimated $U_{\Delta t}$ of the baseline solution ($\Delta t = T_2/1030$) for all quantities of interest are listed in Table 7.

The spatial discretization error was investigated by repeating the simulation with two increasingly finer platform meshes and the baseline time step of $\Delta t = T_2/1030$. The finer (6.2 million cells) and the finest (12.3 million cells) grids were constructed by halving and quartering the reference size, $h_p$ (see Table 3), from the baseline value. The cell thickness in the boundary-layer mesh was also halved and quartered. The size of the platform surface mesh was maintained at $0.5h_p$ for the baseline and finer grids; however, $h_p$ was used for the finest mesh to avoid having an excessive number of cells. It should be noted that the background wave mesh and the free-surface mesh near the platform were kept the same for all cases with $h_w = 0.45$ m because the convergence of the wave mesh was already investigated in Section 4.1. Furthermore, the slight wave dissipation caused by finite grid resolution was already accounted for during wave calibration. Keeping the same background wave mesh has the benefit of maintaining consistent incident waves at the location of the platform, allowing us to focus on the convergence of the near-field flow.

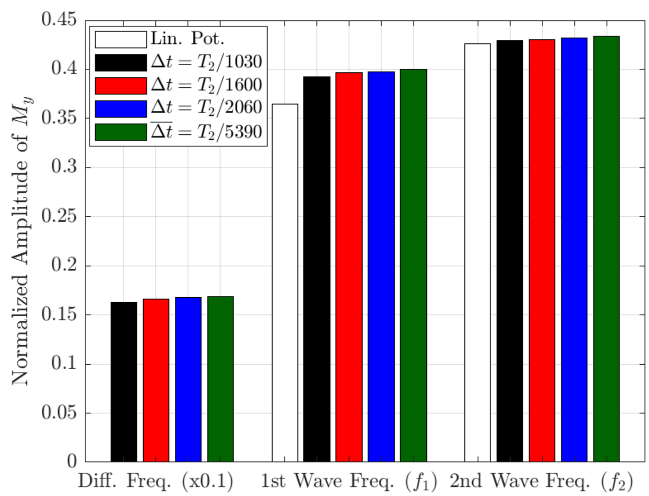

Figure 6. Normalized pitch-moment amplitude at the difference frequency and the two wave frequencies obtained with different time steps (Lin. Pot. = linear potential-flow theory).

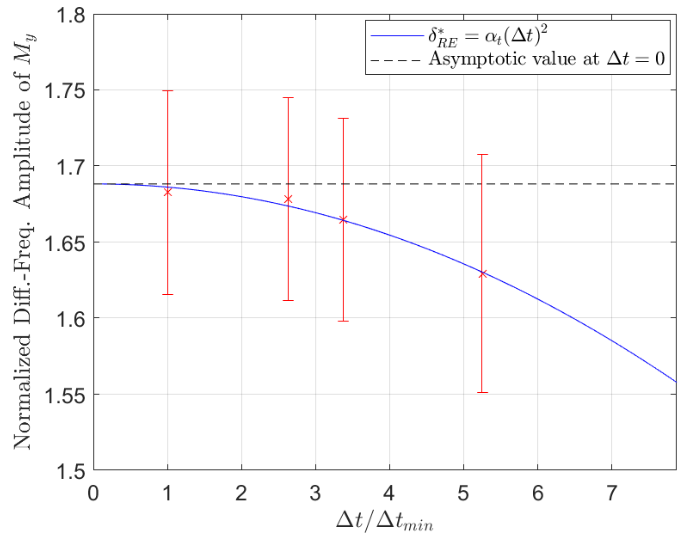

Figure 7. Richardson extrapolation with time step for the normalized pitch-moment amplitude at the difference frequency.

Table 7. Temporal-discretization uncertainties in wave-load amplitudes for the baseline solution.

| | Diff. Freq. ($f_d$) | 1st Wave Freq. ($f_1$) | 2nd Wave Freq. ($f_2$) |
|---|---|---|---|
| $F_x$ | ±5.5% | ±0.7% | ±3.8% |
| $F_z$ | ±13% | ±3.3% | ±5.0% |
| $M_y$ | ±4.9% | ±2.7% | ±1.1% |

As an example, Figure 8 shows the amplitudes of the wave pitch moment computed with the three different grid resolutions. The characteristic cell size near the platform, $h_p$, is expressed as a fraction of the heave-plate diameter, $D = 24$ m. Overall, the change in pitch-moment amplitudes with cell size was small. However, the grid convergence was nonmonotonic, likely because the mesh resolution was not fully in the asymptotic regime and the three grids were not completely geometrically similar. Similar observations were also made for surge and heave forces.

The lack of apparent asymptotic convergence renders the estimation of spatial discretization uncertainty more difficult. Mathematically rigorous approaches based on Richardson extrapolation [28] cannot be reliably applied. Instead, we resorted to the range-based estimation for all spatial discretization uncertainties (i.e., $U_{\Delta x} = 3\Delta_M$, where $\Delta_M$ is the maximum difference in a quantity of interest among the results from all three grids). The large safety factor of 3 reflects the fact that the error estimated based on $\Delta_M$ is not as reliable [29]. Indeed, the reliability of the estimation strongly depends on the available results; $\Delta_M$ can be made artificially small if only very similar grids are considered. In the present work, however, we covered significant changes in cell size in the convergence study; therefore, the range-based estimate should yield an uncertainty estimate that is meaningful. The uncertainty from spatial discretization is listed in Table 8. Generally, $U_{\Delta x}$ is comparable to $U_{\Delta t}$ for the wave-frequency loads but is significantly higher for those at the difference frequency, especially for the heave force. The larger uncertainty reflects the challenges in capturing the small difference-frequency loads with numerical simulations.

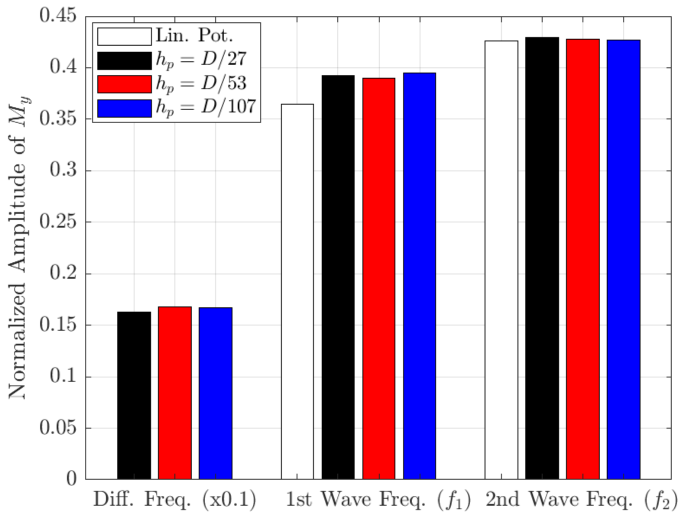


Figure 8. Normalized pitch-moment amplitude at the difference frequency and the two wave frequencies obtained with different cell sizes (Lin. Pot. = linear potential-flow theory).

Table 8. Spatial-discretization uncertainties in wave-load amplitudes for the baseline solution.

| | Diff. Freq. ($f_d$) | 1st Wave Freq. ($f_1$) | 2nd Wave Freq. ($f_2$) |
|---|---|---|---|
| $F_x$ | ±18% | ±2.3% | ±1.4% |
| $F_z$ | ±32% | ±5.2% | ±5.5% |
| $M_y$ | ±9.7% | ±4.3% | ±1.7% |

To obtain the total discretization uncertainty, $U_1$, the estimated temporal and spatial uncertainties listed in Table 7 and Table 8 were conservatively combined through direct summation.

*Modeling uncertainty resulting from the finite domain width*

The uncertainty caused by the finite domain size was primarily controlled by the domain width because the side boundaries were much closer to the platform than the upstream and downstream boundaries. Of course, as discussed in Section 4.1, the overall domain length may affect the difference-frequency free waves that can impact the second-order wave loads. However, it is possible to effectively minimize and subsequently remove the contribution from the free waves by first choosing an appropriate overall domain length and applying the correction procedure described in Section 4.2.2.

The effect of domain width was investigated by repeating the simulation with progressively higher $w_{1/2}$, which is the width of the half domain measured from the platform center plane to the starboard boundary. Four different domain widths from the baseline case of $2w_{1/2}/L = 4$ up to the widest domain of $2w_{1/2}/L = 20$ were considered. The amplitudes of the surge force are shown in Figure 9. For the first and second wave frequencies, the predictions from linear potential-flow theory are also included for reference.

Overall, the predicted force amplitudes were similar across the different cases except for the intermediate domain width of $2w_{1/2}/L = 6$. A significant increase in surge force at the second wave frequency and the difference frequency can be observed. Heave force and pitch moment also showed similar behavior. This was likely caused by the resonance of the diffracted waves at the second wave frequency. The exact resonance mechanism requires further investigation. The results in Figure 9 demonstrate the importance of investigating domain-width effects in numerical wave-tank simulations. The convergence of the results with increasing domain width may not be monotonic because of potential wave resonance, and an improperly chosen domain width may lead to large modeling errors.

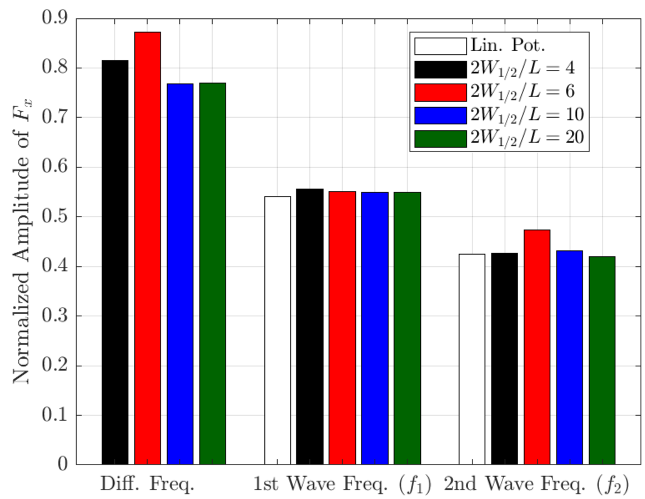


Figure 9. Effect of numerical domain width on the normalized amplitudes of the surge force (Lin. Pot. = linear potential-flow theory).

We multiplied the differences between the results of the baseline setup ($2w_{1/2}/L = 4$) and those of the widest domain ($2w_{1/2}/L = 20$) by a safety factor of 2 to provide an estimate of the modeling uncertainty for the baseline solution. With the intention of establishing a 95% confidence interval, we chose the lower safety factor of 2, compared to 3 used for grid convergence, because the dependence of the various quantities of interest on domain width was expected to be more regular, resulting in a higher degree of confidence in the estimated modeling error. The resulting estimates are listed in Table 9 as percentages of the baseline solution listed in Table 6.

Table 9. Uncertainties in wave-load amplitudes caused by finite domain width.

| | Diff. Freq. ($f_d$) | 1st Wave Freq. ($f_1$) | 2nd Wave Freq. ($f_2$) |
|---|---|---|---|
| $F_x$ | ±12% | ±2.6% | ±2.9% |
| $F_z$ | ±1.8% | ±5.8% | ±6.2% |
| $M_y$ | ±7.8% | ±3.0% | ±1.0% |

*Statistical uncertainty from the fluctuation in load amplitudes*

The uncertainty associated with the fluctuation in force/moment amplitudes over processing time illustrated in Figure 5 can be accounted for by introducing an additional uncertainty, $U_3$. For the sake of consistency among participants, the results from the very last time window (i.e., the values with $t_s = 1.5T_R$) were taken as the final results instead of the mean values (the red dashed line in Figure 5). Therefore, we simply have $U_3 = 2\sigma$, where $\sigma$ is the standard deviation of the fluctuation about the mean. The $\pm 2\sigma$ interval about the mean is shown as a grey band in Figure 5. The values of $U_3$ expressed as percentages of the baseline solution are listed in Table 10. We observed relatively large fluctuation for the difference-frequency heave force. The wave loads at the two wave frequencies all show negligible fluctuation over time.

Table 10. Uncertainties in wave-load amplitudes caused by fluctuation over time.

| | Diff. Freq. ($f_d$) | 1st Wave Freq. ($f_1$) | 2nd Wave Freq. ($f_2$) |
|---|---|---|---|
| $F_x$ | $\pm$4.6% | $\pm$0.4% | $\pm$1.2% |
| $F_z$ | $\pm$14% | $\pm$0.6% | $\pm$1.6% |
| $M_y$ | $\pm$1.8% | $\pm$0.4% | $\pm$0.7% |

*Total Combined Uncertainty*

Finally, the estimated combined uncertainties (approximately 95% confidence), expressed as percentages of the baseline solution in Table 6, are provided in Table 11. The total uncertainties in heave force are considerably higher than those in surge force and pitch moment at all three frequencies. The heave force is strongly influenced by flow separation from the edge of the heave plates. Therefore, it is more sensitive to grid resolution and time step. Furthermore, the presence of strong viscous effects also increases the statistical uncertainty, especially considering the fact that no turbulence model was used to smooth out the flow. At the difference frequency, the uncertainty in heave-force amplitude reached 46%, whereas the more important surge force and pitch moment both have significantly lower uncertainties. Fortunately, the difference-frequency heave force is of little engineering importance. This is because heave resonance frequency is usually much higher for semisubmersibles and fall within the frequency range of linear wave excitation. Low-frequency nonlinear excitation does not play a significant role in heave motion.

Table 11. Total uncertainties in wave-load amplitudes for the baseline solution.

| | Diff. Freq. ($f_d$) | 1st Wave Freq. ($f_1$) | 2nd Wave Freq. ($f_2$) |
|---|---|---|---|
| $F_x$ | $\pm$26% | $\pm$3.9% | $\pm$6.0% |
| $F_z$ | $\pm$46% | $\pm$11% | $\pm$13% |
| $M_y$ | $\pm$17% | $\pm$7.6% | $\pm$3.0% |

### 4.2.2 Correction to Difference-Frequency Forces and Moments

The contributions from the difference-frequency free waves to the second-order wave loads can be subtracted out because the free waves are linear:

$$\tilde{A}_{f,j}(f_d) = A_{f,j}(f_d) - \zeta_{if} X_j(f_d, \theta = 0) - \zeta_{rf} X_j(f_d, \theta = \pi) \quad (9)$$

where $\tilde{A}_{f,j}(f_d)$ and $A_{f,j}(f_d)$ are the corrected and uncorrected force/moment amplitude in the $j$th ($j = 1,2, \ldots,6$) direction at the difference frequency, $f_d$. The complex amplitudes of the incident and reflected free waves, $\zeta_{if}$ and $\zeta_{rf}$, can be obtained from the unobstructed incident wave field using the wave-splitting method described in Section 4.1. Finally, $X_j$ is the unit-amplitude wave-exciting force/moment in the $j$th direction that depends on the wave frequency and incident wave direction, $\theta$ (the angle between the wave direction and the $x$-axis). $X_j$ can be obtained from linear potential-flow theory. Because the amplitudes of the free waves were quite small, any higher-order effect not considered in Eq. (9) should be negligible. This correction procedure was found to be valid based on a limited preliminary study. A more comprehensive evaluation will be performed in the future.

The corrected and normalized amplitudes of difference-frequency wave loads obtained with the baseline configuration are given in Table 12. The corresponding values before the correction are also included for reference. Overall, the correction is significant in heave but relatively minor in surge and pitch.

Table 12. Normalized amplitudes of difference-frequency wave loads before and after correction.

| | Before Correction | After Correction | % change |
|---|---|---|---|
| $F_x$ | 0.8146 | 0.7565 | -7% |
| $F_z$ | 1.7112 | 2.6662 | +56% |
| $M_y$ | 1.6291 | 1.5934 | -2% |

## 5. COMPARISON OF RESULTS FROM PARTICIPANTS AND POTENTIAL-FLOW PREDICTIONS

The CFD predictions of the wave loads from the various participants of the OC6 project are shown in Figures 10–12. The estimated total uncertainties from Section 4.2.1 are added to the results from NREL for reference. The difference-frequency wave loads from the participants have all been corrected with the procedure described in Section 4.2.2. The hatched bars indicate potential-flow predictions. For the two wave frequencies, the linear wave-exciting forces and moments are shown. For the difference frequency, the wave loads predicted by second-order potential-flow QTFs are included.

Overall, the surge force and pitch moment at the two wave frequencies were consistently predicted. The variation across participants is generally small, consistent with the small uncertainty estimate. The CFD predictions for surge force and pitch moment are generally close to, but slightly higher than, those of the linear potential-flow theory for the majority of the participants, indicating only minimal viscous excitation. In contrast, the CFD results for heave force at the lower wave frequency, $f_1$, tend to be significantly higher than the potential-flow prediction, which suggests significant viscous excitation in heave on the large heave plates. The variation in CFD results for the heave force from the various participants is also more pronounced, likely because of the difficulty in accurately resolving the flow separation at the corners of the heave plates. This difficulty is also reflected by the higher uncertainties in NREL results.

Because of the small (unnormalized) magnitudes, accurately capturing the nonlinear difference-frequency loads can be much more challenging. Compared to the wave-frequency loads, the variation in the difference-frequency loads from the participants is generally more significant. Correspondingly, the uncertainty intervals for the NREL results are also wider. Nevertheless, the results from a majority of the OC6 participants show a degree of consistency that is nontrivial for second-order nonlinear loads, especially considering the differences among the numerical setups adopted by the participants. In fact, most participant results lie within the uncertainty band around the NREL results with only a few exceptions. This observation suggests that it may be feasible to consistently predict the nonlinear difference-frequency wave loads on the platform using CFD.

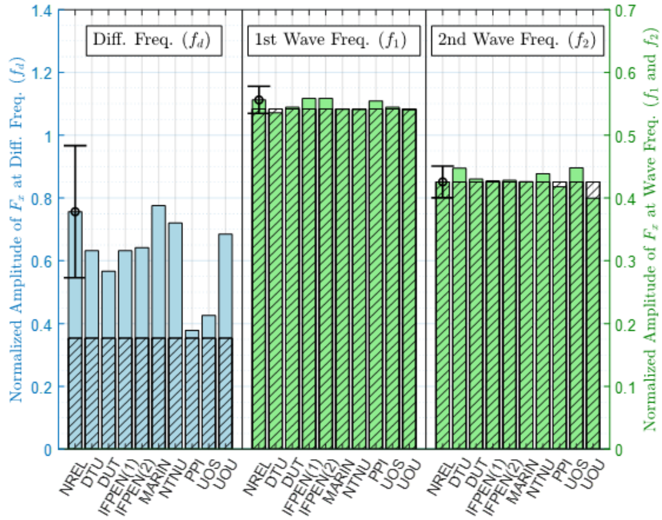


Figure 10. Amplitudes of wave-induced surge force ($F_x$) on the platform at the difference frequency ($f_d$) and wave frequencies ($f_1$ and $f_2$).

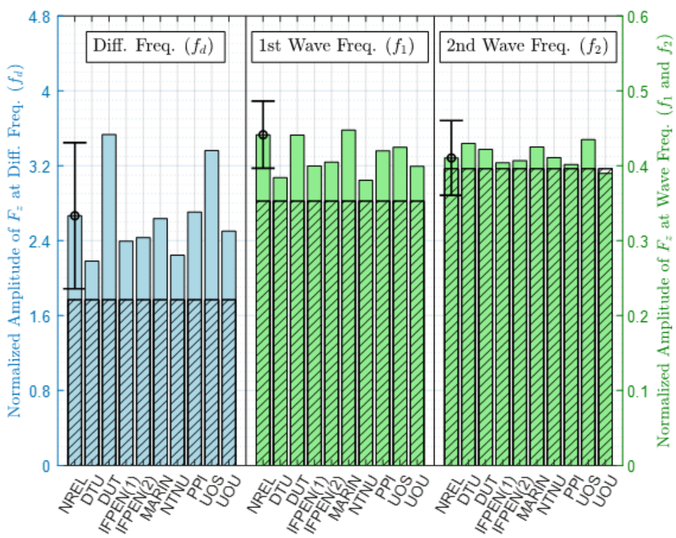


Figure 11. Amplitudes of wave-induced heave force ($F_z$) on the platform at the difference frequency ($f_d$) and wave frequencies ($f_1$ and $f_2$).

The solutions labeled IFPEN(1) and IFPEN(2) were computed using the two different meshes built by IFPEN, as described in Sec. 3.2. IFPEN(1) corresponds to the mesh without the extruded layers, and the simulation was performed with a free-slip condition on the floater. The mesh used to obtain IFPEN(2) included the extruded mesh layers, and a no-slip condition was enforced on the floater. Interestingly, the wave-load amplitudes from the two solutions are very similar. This observation is consistent with the findings in [9] and supports our conjecture that, for the present geometry and wave condition, viscous effects manifest primarily through flow separation from the sharp corners of the heave plate which is insensitive to the finer structures of the boundary layer.

Furthermore, although iteration error was not systematically investigated in this paper, some conjecture can be made by comparing the results from different participants. For example, MARIN used a stopping criterion of $10^{-6}$ residual reduction up to a maximum of 100 outer iterations, whereas NREL fixed the number of iterations per time step to 20. Despite the difference in the stopping criteria for outer iterations, wave loads from MARIN and NREL are in good agreement, including at the difference frequency. It is, therefore, reasonable to assume that iteration error, compared to other sources of error, would not play a significant role in the total uncertainty for the baseline setup. Of course, there were other differences between MARIN and NREL simulations that could potentially "negate" the effect of the difference in iteration error. For example, MARIN used an upstream wave-forcing zone, whereas NREL did not. Therefore, a more robust quantification of the iteration uncertainty would require a systematic analysis in the future.

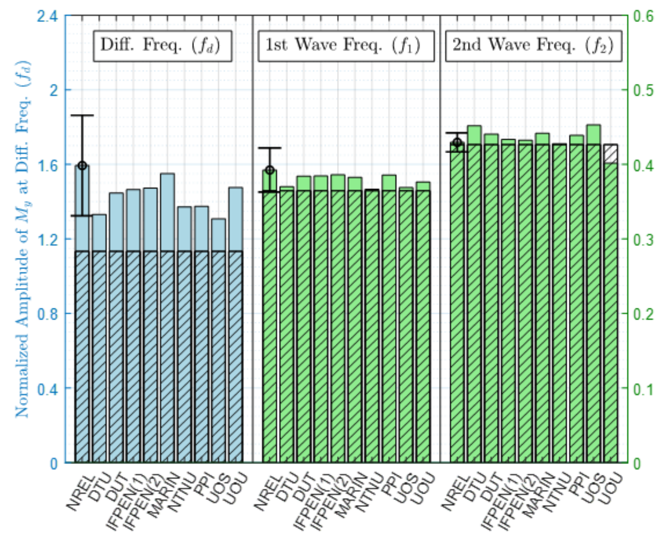


Figure 12. Amplitudes of wave-induced pitch moment ($M_y$) on the platform at the difference frequency ($f_d$) and wave frequencies ($f_1$ and $f_2$).

The difference-frequency loads predicted by potential-flow QTFs are, for the most part, below CFD predictions, even considering the uncertainties in the CFD results. It may, therefore, be beneficial to calibrate the engineering models of offshore wind platforms, which were found to frequently underpredict low-frequency loads and responses [5], using the CFD results of a collection of strategically selected bichromatic-wave cases.

## 6. CONCLUSIONS

As part of Phase I of the OC6 project, the feasibility of estimating nonlinear low-frequency wave loads on a semisubmersible offshore wind platform using CFD was investigated collaboratively. We simulated a fixed platform in bichromatic incident waves. The use of bichromatic waves with a short repeat period, instead of irregular waves, shortens the physical time that needs to be simulated, significantly reducing the computing time. The resulting difference-frequency load can also be directly compared to the quadratic transfer functions from second-order potential-flow theory.

We performed a numerical convergence study and a systematic evaluation of uncertainty for the CFD results from NREL. Sources of uncertainty considered included numerical space and time discretization, effect of finite domain size, and statistical uncertainty caused by the fluctuation of force/moment amplitudes over the analysis range. CFD predictions of surge-force and pitch-moment amplitudes at the two wave frequencies were found to have relatively low uncertainty, and the CFD results were close to those of linear potential-flow theory, indicating minimal viscous effects on those force components. Higher uncertainty was estimated for the wave-frequency heave force, which showed significant contribution from viscous excitation. The higher uncertainty in heave force reflects the difficulty, which arises from the numerical resolution required, in accurately capturing the flow separation from the heave plates.

Predicting the nonlinear difference-frequency wave loads is also considerably more challenging because of the smaller magnitudes. The relative uncertainties in the difference-frequency loads were also correspondingly higher. Nevertheless, the CFD results from the participants were consistently higher than potential-flow QTFs even with uncertainties considered. Therefore, CFD results of a collection of strategically selected bichromatic-wave cases have the potential to be used to calibrate the engineering models of offshore wind platforms, which often suffer from the underprediction of nonlinear low-frequency wave loads and platform responses.

The team also compared the CFD results from the participants of the OC6 project to each other. Interestingly, the variation among the participant results was largely consistent with the estimated uncertainty. As expected, the relative variation in difference-frequency loads was more significant; however, most participant results agreed with the results from NREL to within the estimated uncertainty. This level of agreement is nontrivial, considering the difference among the numerical setups adopted by the participants. This observation suggests that CFD can provide consistent estimates of the nonlinear low-frequency wave loads on a semisubmersible offshore wind platform. Of course, validation of those results can only be achieved when comparison with wave-basin experiments is done. An experimental validation campaign designed for this purpose is planned for the near future.

## ACKNOWLEDGEMENTS

This work was authored in part by the National Renewable Energy Laboratory, operated by Alliance for Sustainable Energy, LLC, for the U.S. Department of Energy (DOE) under Contract No. DE-AC36-08GO28308. Funding provided by the U.S. Department of Energy Office of Energy Efficiency and Renewable Energy Wind Energy Technologies Office. The views expressed in the article do not necessarily represent the views of the DOE or the U.S. Government. The U.S. Government retains and the publisher, by accepting the article for publication, acknowledges that the U.S. Government retains a nonexclusive, paid-up, irrevocable, worldwide license to publish or reproduce the published form of this work, or allow others to do so, for U.S. Government purposes.

A portion of the research was performed using computational resources sponsored by DOE's Office of Energy Efficiency and Renewable Energy and located at the National Renewable Energy Laboratory.

MARIN would like to acknowledge that this research is partly funded by the Dutch Ministry of Economic Affairs.

PPI acknowledges École Centrale Marseille and the Centre de Calcul Intensif d'Aix-Marseille for granting access to their high-performance computing resources.

## REFERENCES

[1] Simos, A. N., Sparano, J. V., Aranha, J. A. P. and Matos, V. L. F., (2008), "2nd order hydrodynamic effects on resonant heave, pitch and roll motions of a large-volume semi-submersible platform," in *Proceedings of the ASME 27th International Conference on Offshore Mehcanics and Arctic Engineering*, pp. 229-237.

[2] Bayati, I., Jonkman, J., Robertson, A. and Platt, A., (2014), "The effects of second-order hydrodynamics on a semisubmersible floating offshore wind turbine," *Journal of Physics: Conference Series,* Vol. 524, p. 012094.

[3] Robertson, A. et al., (2017), "OC5 Project Phase II: Validation of global loads of the DeepCwind floating semisubmersible wind turbine," *Energy Procedia,* Vol. 137, pp. 38-57.

[4] Simos, A. N., Ruggeri, F., Watai, R. A., Souto-Iglesias, A. and Lopez-Pavon, C., (2018), "Slow-drift of a floating wind turbine: An assessment of frequency-domain methods based on model tests," *Renewable Energy,* Vol. 116, pp. 133-154.

[5] Robertson, A. et al., (2020), "OC6 Phase I: Investigating the under-prediction of low-frequency hydrodynamic loads and responses of a floating wind turbine," in *Proceedings of the EAWE's TORQUE 2020 Conference*.

[6] U. S. Department of Energy (DOE), "OC6 - Offshore Code Comparison Collaboration, Continued, with Correlation and unCertainty," [Online]. Available: https://a2e.energy.gov/projects/oc6.

[7] Tran, T. T. and Kim, D. H., (2015), "The coupled dynamic response computation for a semi-submersible platform of floating offshore wind turbine," *Journal of Wind Engineering and Industrial Aerodynamics,* Vol. 147, pp. 104-119.

[8] Sarlak, H., Pegalajar-Jurado, A. and Bredmose, H., (2018), "CFD simulations of a newly developed floating offshore wind turbine platform using OpenFOAM," in *Proceedings of the 21st Australasion Fluid Mechanics Conference*.

[9] Clément, C., Bozonnet, P., Vinay, G., Borràs Nadal, A., Pagnier, P. and Réveillon, J., (2020), "Numerical wave tank including a fixed vertical cylinder subjected to waves, towards the investigation of floating offshore wind turbine hydrodynamics," in *Proceedings of ASME 2020 39th International Conference on Ocean, Offshore and Arctic Engineering*.

[10] Ren, N., Li, Y. and Ou, J., (2014), "Coupled wind-wave time domain analysis of floating offshore wind turbine based on Computational Fluid Dynamics method," *Journal of Renewable and Sustainable Energy,* Vol. 6, p. 023106.

[11] Burmester, S., Vaz, G., Gueydon, S. and el Moctar, O., (2020), "Investigation of a semi-submersible floating wind turbine in surge decay using CFD," *Ship Technology Research,* Vol. 67, No. 1, pp. 2-14.

[12] Bozonnet, P. and Emery, A., (2015), "CFD simulations for the design of offshore floating wind platforms encompassing heave plates," in *Proceedings of the 25th International Ocean and Polar Engineering Conference*.

[13] Tran, T. T. and Kim, D. H., (2016), "Fully coupled aero-hydrodynamic analysis of a semi-submerisble FOWT using a dynamic fluid body interation approach," *Renewable Energy,* Vol. 92, pp. 244-261.

[14] Zhang, Y. and Kim, B., (2018), "A fully coupled computational fluid dynamics method for analysis of semi-submersible floating offshore wind turbines under wind-wave excitation conditions based on OC5 data," *Applied Science,* Vol. 8, No. 11, p. 2314.

[15] Liu, Y., Xiao, Q., Incecik, A., Peyrard, C. and Wan, D., (2017), "Establishing a fully coupled CFD analysis tool for floating offshore wind turbines," *Renewable Energy,* Vol. 112, pp. 280-301.

[16] Tom, N., Robertson, A., Jonkman, J. and Wendt, F., (2019), "Bichromatic wave selection for validation of the difference-frequency transfer function for the OC6 validation campaign," in *Proceedings of the 2nd International Offshore Wind Technical Conference*.

[17] Shao, Y.-L. and Faltinsen, O. M., (2014), "A numerical study of the second-order wave excitation of ship springing by a higher-order boundary element method," *International Journal of Naval Architecture and Ocean Engineering,* Vol. 6, No. 4, pp. 1000-1013.

[18] Weller, H. G., Tabor, G., Jasak, H. and Fureby, C., (1998), "A tensorial approach to computational continuum mechanics using object-oriented techniques," *Computers in Physics,* Vol. 12, No. 6, pp. 620-631.

[19] Jacobsen, N. G., Fuhrman, D. R. and Fredsøe, J., (2012), "A wave generation toolbox for the open-source CFD library: OpenFoam®," *International Journal for Numerical Methods in Fluids,* Vol. 70, No. 9, pp. 1073-1088.

[20] Bruinsma, N., Paulsen, B. T. and Jacobsen, N. G., (2018), "Validation and application of a fully nonlinear numerical wave tank for simulating floating offshore wind turbines," *Ocean Engineering,* Vol. 147, pp. 647-658.

[21] NUMECA International, (2019), HEXPRESS, Unstructured Full-Hexahedral Meshing.

[22] ReFRESCO, (2020), ReFRESCO v2.6.0 Documentation.

[23] Klaij, C. M., Hoekstra, M. and Vaz, G., (2018), "Design, analysis and verification of a volume-of-fluid model with interface-capturing scheme," *Computers and Fluids,* Vol. 170, pp. 324-340.

[24] Siemens PLM Software, (2018), Simcenter STAR-CCM+ User Guide, Version 13.06.012.

[25] ANSYS Inc., (2018), ANSYS Fluent 19.2 User Guide.

[26] Waals, O. J., (2009), "On the application of advanced wave analysis in shallow water model testing (wave splitting)," in *Proceedings of the ASME 28th International Conference on Ocean, Offshore and Arctic Engineering*, pp. 415-423.

[27] Ogilvie, T. F., (1983), "Second-order hydrodynamic effects on ocean platforms," in *Proceedings of the International Workshop on Ship and Platform Motions*, pp. 205-265.

[28] Eça, L., (2006), "On the influence of the iterative error in the numerical uncertainty of ship viscous flow calculations," in *Proceedings of the 26th Symposium on Naval Hydrodynamics*.

[29] Eça, L. and Hoekstra, M., (2014), "A procedure for the estimation of the numerical uncertainty of CFD calculations based on grid refinement studies," *Journal of Computational Physics,* Vol. 262, pp. 104-130.

[30] Eça, L. and Hoekstra, M., (2009), "Evaluation of numerical error estimation based on grid refinement studies with the method of the manufactured solutions," *Computers & Fluids,* Vol. 38, pp. 1580-1591.

## APPENDIX: CFD SETTINGS OF OC6 PARTICIPANTS

Table A.1. CFD Settings of OC6 Participants.

| Participant | Software | Discretization[1] | | | | Pressure-Velocity Coupling | | | | Boundary Conditions[2] | | Wave Forcing/Relaxation/ Damping Zones | | Volume Fraction Transport Scheme[3] |
|---|---|---|---|---|---|---|---|---|---|---|---|---|---|---|
| | | Time Step | Boundary-Layer Mesh | | | Algorithm | Stopping Criteria | | | Downstream | Floater | Upstream Type/Length | Downstream Type/Length | |
| | | | Number of Layers | First-Layer Thickness | Overall Thickness | | No. of Press. Corr. | Residual Tolerance | Max. Iterations | | | | | |
| DTU Tech. Univ. Denmark | OpenFOAM ver. 1812 waves2Foam | $T_2/1030$ | N/A | N/A | N/A | PISO | 3 | N/A | N/A | Const. Pressure | No Slip | Forcing/ $1.5\lambda_1$ | Damping/ $2.0\lambda_1$ | MULES |
| DUT Dalian Univ. Tech. | STAR-CCM+ ver. 13.06.012 | $T_2/1030$ | 10 | 0.001m | 0.4m | SIMPLE | N/A | None | 20 | Wave Velocity | No Slip | Forcing/ $1.5\lambda_1$ | Relaxation/ $1.5\lambda_1$ | HRIC |
| IFPEN(1) IFP Energies nouvelles | OpenFOAM ver. 1812 waves2Foam | $T_2/1030$ | N/A | N/A | N/A | PISO | 3 | N/A | N/A | Wave Velocity | Free Slip | Forcing/ $0.5\lambda_1$ | Relaxation/ $2.0\lambda_1$ | MULES |
| IFPEN(2) IFP Energies nouvelles | OpenFOAM ver. 1812 waves2Foam | $T_2/1030$ | 5 | 0.0675m | 0.3375m | PISO | 3 | N/A | N/A | Wave Velocity | No Slip | Forcing/ $0.5\lambda_1$ | Relaxation/ $2.0\lambda_1$ | MULES |
| MARIN Maritime Research Inst. Netherlands | ReFRESCO | $T_2/1030$ | 10 | 0.001m | 0.4m | SIMPLE | N/A | $10^{-6}$ | 100 | Sommerfeld for Diff. Freq. | No Slip | Forcing/ $1.5\lambda_1$ | Relaxation/ $3.0\lambda_1$ | ReFRICS |
| NREL National Renewable Energy Laboratory | STAR-CCM+ ver. 13.06.012 | $T_2/1030$ | 10 | 0.001m | 0.4m | SIMPLE | N/A | None | 20 | Const. Pressure | No Slip | None | Damping/ $2.0\lambda_1$ | HRIC |
| NTNU Norwegian Univ. of Sci. & Tech. | OpenFOAM ver. 1712 waves2Foam | $T_2/1030$ | 10 | 0.001m | 0.4m | PISO | 3 | N/A | N/A | Const. Pressure | No Slip | Forcing/ $1.0\lambda_1$ | Damping/ $4.0\lambda_1$ | MULES |
| PPI Principle Power, Inc. | OpenFOAM ver. 1812 waves2Foam | $T_2/1030$ | N/A | N/A | N/A | PISO | 3 | N/A | N/A | Wave Velocity | No Slip | Forcing/ $1.5\lambda_1$ | Relaxation/ $2.0\lambda_1$ | MULES |
| UOS Univ. Strathclyde | OpenFOAM ver. 4.x waves2Foam | $T_2/2438$ | N/A | N/A | N/A | PIMPLE | 2 | $10^{-8}$ | 10 | Wave Velocity | No Slip | Forcing/ $1.5\lambda_1$ | Relaxation/ $4.0\lambda_1$ | MULES |
| UOU Univ. Ulsan | ANSYS Fluent ver. 19.2 | $T_2/862$ | 10 | 0.001m | 0.4m | SIMPLE | N/A | None | 35 | Const. Pressure | No Slip | None | Damping/ $2.0\lambda_1$ | CICSAM |

**1.** The cell sizes outside the boundary-layer region follows the baseline setup described in Section 3.1. One exception was NTNU which halved the cell size in the $y$-direction on the free surface (first mesh refinement region in Table 2). Second order spatial and temporal (implicit) discretization was used except DTU which used the backward Euler method for time integration.

**2.** The boundary conditions on the other boundaries were standard as described in Section 3.

**3.** The algorithms used were the Multi-Dimensional Limiter for Explicit Solution (MULES), High-Resolution Interface-Capturing (HRIC) scheme, the Compressive Interface Capturing Scheme for Arbitrary Meshes (CICSAM), and ReFRICS [23].